Monthly Notices
of the
ROYAL ASTRONOMICAL SOCIETY

MNRAS **494,** 571–583 (2020)
Advance Access publication 2020 March 18

doi:10.1093/mnras/staa739

On the nature of the soft γ-ray emission in the hard state of the black hole transient GRS 1716−249

T. Bassi [1,2,3★] J. Malzac,[3★] M. Del Santo,[1★] E. Jourdain,[3] J.-P. Roques,[3] A. D'Aì [1] J. C. A. Miller-Jones [4] R. Belmont,[5] S. E. Motta [6] A. Segreto,[1] V. Testa[7] and P. Casella[7]

[1]*INAF – Istituto di Astrofisica Spaziale e Fisica Cosmica di Palermo, Via Ugo La Malfa 153, I-90146 Palermo, Italy*
[2]*Dipartimento di Fisica e Chimica – Emilio Segré, Universitá degli Studi di Palermo, via Archirafi 36, I-90123 Palermo, Italy*
[3]*IRAP, Université de Toulouse, CNRS, UPS, CNES, Toulouse, France*
[4]*International Centre for Radio Astronomy Research, Curtin University, GPO Box U1987, Perth, WA 6845, Australia*
[5]*AIM, CEA, CNRS, Université Paris-Saclay, Université Paris Diderot, Sorbonne Paris Cité, F-91191 Gif-sur-Yvette, France*
[6]*Department of Physics, Astrophysics, University of Oxford, Denys Wilkinson Building, Keble Road, Oxford OX1 3RH, UK*
[7]*INAF, Osservatorio Astronomico di Roma, Via Frascati 33, I-00078 Monteporzio Catone, Roma, Italy*

Accepted 2020 March 13. Received 2020 March 13; in original form 2020 January 15

ABSTRACT

The black hole transient GRS 1716−249 was monitored from the radio to the γ-ray band during its 2016–2017 outburst. This paper focuses on the spectral energy distribution (SED) obtained in 2017 February–March, when GRS 1716−249 was in a bright hard spectral state. The soft γ-ray data collected with the *INTEGRAL*/SPI telescope show the presence of a spectral component that is in excess of the thermal Comptonization emission. This component is usually interpreted as inverse Compton emission from a tiny fraction of non-thermal electrons in the X-ray corona. We find that hybrid thermal/non-thermal Comptonization models provide a good fit to the X-/γ-ray spectrum of GRS 1716−249. The best-fitting parameters are typical of the bright hard state spectra observed in other black hole X-ray binaries. Moreover, the magnetized hybrid Comptonization model BELM provides an upper limit on the intensity of the coronal magnetic field of about 10^6 G. Alternatively, this soft γ-ray emission could originate from synchrotron emission in the radio jet. In order to test this hypothesis, we fit the SED with the irradiated disc plus Comptonization model combined with the jet internal shock emission model ISHEM. We found that a jet with an electron distribution of $p \simeq 2.1$ can reproduce the soft γ-ray emission of GRS 1716−249. However, if we introduce the expected cooling break around 10 keV, the jet model can no longer explain the observed soft γ-ray emission, unless the index of the electron energy distribution is significantly harder ($p < 2$).

Key words: accretion, accretion discs – black hole physics – ISM: jets and outflows – gamma-rays: general – X-rays: binaries.

1 INTRODUCTION

Black hole X-ray binaries (BHBs) are binary systems where a BH accretes material from an ordinary star. In these systems, the X-ray emission originating from the accretion flow can reach X-ray luminosities of $L_X \sim 10^{36–39}$ erg s^{-1}. While a few BHBs are persistent (characterized by steady X-ray emission), most of them are transient sources (called black hole transients, BHTs), i.e. they alternate long periods in a low-luminosity quiescent state with episodic outbursts. Furthermore, BHBs are associated with powerful jets whose synchrotron emission is usually observed in the radio and infrared bands. Based on X-ray spectral and timing properties, it is possible to identify characteristic spectral states (Zdziarski & Gierliński 2004; Remillard & McClintock 2006). In particular, the hard state (HS) is characterized by a dominating hard-X energy spectrum, interpreted as thermal Comptonization of soft disc photons by a hot plasma ($kT_e \sim$ 50–100 keV) located close to the BH (Zdziarski & Gierliński 2004). A weak soft thermal component (inner disc blackbody temperature of ∼0.1–0.2 keV), possibly originating from the accretion disc truncated at large radii (roughly 100 R_g) from the BH (Done, Gierliński & Kubota 2007), is also observed. A high fractional root mean squared (rms)

★ E-mail: bassi@ifc.inaf.it (TB); Julien.Malzac@irap.omp.eu (JM); melania@ifc.inaf.it (MDS)

variability (as high as 30 per cent, Muñoz-Darias, Motta & Belloni 2011; Belloni & Motta 2016) also characterizes hard spectral states.

A flat or slightly inverted ($F_\nu \propto \nu^\alpha$ with $\alpha \sim 0.5$–0) radio/infrared (IR) spectrum is generally observed in the HS. This is interpreted as partially self-absorbed synchrotron emission from relativistic electrons ejected from the system through collimated compact jets (Corbel et al. 2000; Fender et al. 2000; Corbel & Fender 2002), analogous to what is observed in active galactic nuclei (AGNs; Blandford & Königl 1979). However, a dissipation mechanism compensating for the adiabatic losses is required to maintain the flat spectral shape, otherwise we would observe a strongly inverted radio spectrum. Malzac (2013, 2014) showed that the internal shocks caused by fast fluctuations of the jet velocity can be an effective dissipation mechanism along the jets. The origin of the fluctuations is likely driven by the variability of the accretion flow. In this framework, Drappeau et al. (2017) suggested that the drop of the radio/IR emission in the soft spectral state, usually ascribable to the quenching of the jets (Fender et al. 1999; Corbel et al. 2000), might be associated with the low X-ray variability (rms < 5 per cent) that characterizes this spectral state.

In recent years, a further component has been observed by the *INTEGRAL* satellite in a number of BHBs, in addition to the thermal Comptonization emission dominating the X-ray spectra of the HSs (e.g. Del Santo et al. 2008; Bouchet et al. 2009; Del Santo et al. 2016). The first evidence of soft γ-ray emission above ∼200 keV was observed in a few bright BHBs (Nolan et al. 1981; Johnson et al. 1993; Roques et al. 1994). Moreover, observations performed with the COMPTEL telescope showed that this component extends above 1 MeV in Cyg X–1 (McConnell et al. 1994, 2002). Usually, this component is explained as a Comptonization process due to a non-thermal electron population in the corona (Poutanen & Coppi 1998; Coppi 1999; Gierliński et al. 1999; Malzac & Belmont 2009). Alternative scenarios invoke proton–proton π^0 decay emission (Jourdain & Roques 1994), or spatial/temporal variation of the thermal electrons' plasma parameters (Malzac & Jourdain 2000). Recent measurements of strongly polarized emission above 250 keV in Cyg X–1 have provided support to the hypothesis that a synchrotron process in the jet environment is a possible origin of this component (Laurent et al. 2011; Jourdain et al. 2012; Rodriguez et al. 2015). Studies performed on Cyg X–1 in the *Fermi* energy band (above a few hundred MeV) have shown that this emission can be explained in terms of synchrotron self-Compton (SSC) processes (Zdziarski et al. 2017). On the other hand, it can also be well reproduced by jet models assuming continuous particle acceleration along the jet, even though a very hard electron energy distribution (electron index ∼1.5) and strong constraints on the magnetic field are required (Zdziarski et al. 2014b).

The BHT GRS 1716−249 (GRO J1719−24 or Nova Oph 1993) was discovered by the *CGRO*/BATSE and *Granat*/SIGMA telescopes during an outburst that occurred in 1993 September (Ballet et al. 1993; Harmon et al. 1993). The orbital period was estimated as 14.7 h and a lower limit of 4.9 $M_\odot$ for the mass of the compact object was reported by Masetti et al. (1996), confirming the BHT nature of the source. Radio observations indicated a flat radio spectrum (Della Valle et al. 1993; Della Valle, Mirabel & Rodriguez 1994).

After more than 20 yr in quiescence, GRS 1716−249 was observed again in outburst by *MAXI* (Masumitsu et al. 2016; Negoro et al. 2016). Bassi et al. (2019) reported on the GRS 1716−249 outburst monitoring, performed both in the radio band with the Australia Telescope Compact Array (ATCA), the Karl G. Jansky Very Large Array (VLA), and the Australian Long Baseline Array (LBA), and in X-rays with the XRT and Burst Alert Telescope (BAT) telescopes on board the *Neil Gehrels Swift Observatory* (hereafter *Swift*). During this outburst (lasting about 1 yr), GRS 1716−249 showed only the spectral characteristics of the hard and hard-intermediate states. Recently, Tao et al. (2019) inferred a disc inclination angle in the range 40°–50°. The radio observations indicated that the emission could originate in a compact jet, despite the accretion disc being possibly at the innermost stable circular orbit (ISCO), or with the hot accretion flow having re-condensed in an inner mini-disc (Bassi et al. 2019). Moreover, it was observed that GRS 1716−249 was located on the radio-quiet branch ($L_R \propto L_X^{1.4}$, Coriat et al. 2011) on the radio/X-ray luminosity plane during the whole outburst.

In this paper, we present results of our multiwavelength campaign (from radio to γ-rays), performed in 2017 February when the source was in a bright hard spectral state. Our aim was understanding the nature of the soft γ-ray emission (≥200 keV), also observed in other sources. We detected this emission with the SPI telescope and applied different models to investigate its origin.

2 OBSERVATIONS AND DATA REDUCTION

On 2017 February 9, when GRS 1716−249 was in a bright HS, a multiwavelength campaign was performed offering a sampling of observations from radio to γ-rays. The source was simultaneously observed with *INTEGRAL*, *Swift*, the Rapid Eye Mount Telescope (REM), and the ATCA. The ATCA data reduction has already been reported in Bassi et al. (2019), where we measured flux densities of 3.28 ± 0.05 mJy at 5.5 GHz and of 3.04 ± 0.03 mJy at 9 GHz. The radio spectral index $\alpha = -0.15 \pm 0.08$ was consistent with a flat-spectrum compact jet (Bassi et al. 2019).

2.1 REM near-IR observations

Observations in the near-IR filters *J*, *H*, and *K* were obtained with the 60-cm robotic telescope REM located at the ESO-La Silla Observatory, and equipped with the IR camera REMIR (Vitali et al. 2003). The instrument has a field of view (FOV) of ∼10 arcmin × 10 arcmin and a 512-pixel camera with a pixel scale of 1.1 arcsec per pix. Observations and preliminary reductions and calibrations are done in a completely automated way by the robotic system using the pipeline AQuA (Automatic QUick Analysis, Testa et al. 2004), and pre-processed images and initial catalogues are archived and then distributed to the program PIs. Observations of GRS 1716−249 were performed during the night of 2017 February 9, by acquiring one single observation in the *J* and *H* filters, and two points in the *K* filter. The acquisition strategy is based on a series of frames acquired by rotating a filter wedge along the optical path in order to obtain five displaced images that are then combined together to obtain an 'empty sky' image of the field by median filtering the single images, that is then subtracted from the original frames. The sky-subtracted, flat-fielded frames are then registered together and summed to obtain the final science image. By using this pipeline, the final images have exposure times of 300, 150, and 75 s for the *J*, *H*, and *K* filters, respectively. The final science frames were reduced and analysed using PSF-fitting photometry package DAOPHOT (Stetson et al. 1989; Stetson 1994) and calibrated with the 2MASS survey by matching the 2MASS catalogue with the output DAOPHOT list after transforming the image coordinates into RA, Dec. couples by using the astrometric information available in the header and obtained during the observation from the automatic

Table 1. REM and *Swift*/UVOT start time of the observations analysed in this work, in Terrestrial Time (TT) and MJD. In the columns are reported the exposure time and the filters used. In the last column are reported the REM magnitudes and the UVOT flux density in units of 10^{-16} erg s^{-1} cm^{-2} Å^{-1} for each filter.

Date (TT)	MJD	Exposure (s)	Filter	Magnitude/flux
2017-02-09T07:47:00.384	57793.32466	300.0	*J*	14.18 ± 0.22
2017-02-09T07:52:33.542	57793.32834	150.0	*H*	13.81 ± 0.14
2017-02-09T07:56:11.098	57793.33077	75.0	*K*	13.84 ± 0.29
2017-02-09T07:58:12.403	57793.33218	75.0	*K*	13.59 ± 0.16
2017-02-09T18:11:07	57793.76	109	*U*	4.8 ± 0.5
		109	*B*	6.5 ± 0.6
		109	*V*	9.3 ± 1.0
		217	*UW*1	1.68 ± 0.34
		436	*UW*2	<1.19
		339	*UV*2	<1.46

REM pipeline. The single measurements for each night and for each filter were then matched together and the final results are shown in Table 1.

2.2 Swift observations

On 2017 February 9, six observations were performed with the X-Ray Telescope (XRT; Burrows et al. 2005) and the Ultraviolet/Optical Telescope (UVOT; Roming et al. 2005) on board *Swift* (Gehrels et al. 2004). The data were processed using the FTOOLS software package in HEASOFT v.6.26 and the *Swift* relative Calibration Database (CALDB). The criteria adopted for the pile-up correction and the source spectrum extraction were performed as described in Bassi et al. (2019). To apply the χ^2 statistics, the energy channels were grouped to have at least 50 counts per energy bin. The average XRT spectrum obtained from the six observations performed was strongly affected by the known strong instrumental silicon (1.84 keV) and gold (2.2 keV) edges[1]. Therefore, we decided to use only one of the six spectra of GRS 1716−249 in the spectral analysis described in the next sections. We have made sure that the spectral parameters and the fluxes of the six observations were consistent with each other, and we selected the pointing 00034924012.

By combining the six XRT observations taken on February 9 we extracted and averaged the power density spectrum (PDS), using custom software written in IDL[2]. We used ≈29-s long intervals and a Nyquist frequency of ≈64 Hz, and from each interval we computed a PDS in the energy band 0.4–10.0 keV. We then averaged the PDSs and we normalized the result according to rms^2/Hz normalization.

Furthermore, we determined magnitudes and fluxes for UVOT images using the task UVOTSOURCE, selecting a circular region of 5 arcsec at the best source coordinates and a larger region with no other source as background. The flux densities calculated in the different bands for each observation are reported in Table 1.

From 2016 December 1 (MJD 57723), GRS 1716−249 was observed almost daily in survey mode with the BAT (Barthelmy et al. 2005). To increase the statistics of the BAT spectrum, we selected the GRS 1716−249 observations (available from the HEASARC public archive) performed from 2017 February 2 (MJD 57786) to March 15 (MJD 57827), when the source was constant in flux and spectral shape in hard X-rays (Bassi et al. 2019). The data were processed using the BAT-IMAGER software (Segreto et al. 2010). We extracted the spectrum in 29 channels with logarithmic binning in the energy range 15–185 keV. The official BAT spectral redistribution matrix was used.

2.3 INTEGRAL observations

We collected and analysed the *INTEGRAL* (Winkler et al. 2003) ToO campaign data performed on February 9 and all public observations of GRS 1716−249 from 2017 February 2 to March 15 (from revolution 1780 up to 1793).

The SPI (Vedrenne et al. 2003) analysis was performed using the SPI Data Analysis Interface (SPIDAI) tools[3]. The SPI camera records the signal contribution from the sources in the FOV plus the background. To correctly describe the data, we introduced some information on these components. We assumed a constant background during 12 Science Windows (SCW). The sky models were determined based on the IBIS/ISGRI map of each SCW within the revolution and of the full revolution. We selected the most significant sources ($\sigma \geq 10$) present in the SPI FOV during each revolution. The sources' variability was defined by their IBIS/ISGRI light curves within the SCW binning time (1 SCW∼ h).

The GRS 1716−249 SPI spectrum for each revolution was extracted in 39 channels in the energy range 25–1000 keV, requiring at least 2σ significance in the higher energy bin (i.e. ≥300 keV).

3 BROAD-BAND X/γ-RAY SPECTRAL MODELLING

The spectral variability study based on XRT and BAT data has been reported by Bassi et al. (2019). The authors did not observe any significant variability in the day-averaged emission of the source up to the 150 keV energy band from MJD 57786 to MJD 57827.

To investigate the variability above 150 keV, we fitted the SPI spectrum of each revolution with a CUTOFFPL model. We observed that the photon index and high energy cut-off values were consistent within the errors and the flux variation in the 25–300 keV energy band was lower than about 20 per cent. Moreover, we did not

[1] https://heasarc.gsfc.nasa.gov/docs/heasarc/caldb/swift/docs/xrt/SWIFT-XRT-CALDB-09_v19.pdf

[2] GHATS, http://www.brera.inaf.it/utenti/belloni/GHATS_Package/Home.html

[3] http://sigma-2.cesr.fr/integral/spidai

observe any significant spectral variability in the energy range 200–600 keV: i.e. the hardness ratio [300–600] keV/[200–300] keV (with a revolution time bin) is constant.

Therefore, it was possible to use the averaged BAT and SPI spectra from MJD 57786 to MJD 57827 (2017 February 2 to March 15) with the XRT pointing (MJD 57793.76) to perform a broad-band spectral analysis in the largest energy range possible.

The spectra were fitted with XSPEC v. 12.9.1p. All the errors reported are at the 90 per cent confidence level. A systematic error of 2 per cent was introduced in all the broad-band spectra. In the fits we adopted the cosmic abundances of Wilms, Allen & McCray (2000) and the cross-sections of Verner et al. (1996).

Even though we obtained a good χ^2 (χ^2_ν(dof) = 1.05(336)) applying an absorbed thermal Comptonization model (TBABS plus NTHCOMP in XSPEC), we observed significant residuals above 200 keV. The addition of a power-law component at high energy allows us to eliminate these residuals and improve the fit (χ^2_ν(dof) = 0.97(334)), with a F-test probability 2.32×10^{-6}.

We found a hydrogen column density $N_{\rm H} = 0.70 \pm 0.02 \times 10^{22}\,{\rm cm}^{-2}$, a photon index $\Gamma = 1.68 \pm 0.01$, and an electron temperature $kT_{\rm e} = 50^{+4}_{-3}$ keV, consistent with the values reported in Bassi et al. (2019). Then, we observed that a power law with photon index $\Gamma = 1.12^{+0.21}_{-0.63}$ reproduces the high energy excess above 200 keV and a flux of $F_{[200-600]\,{\rm keV}} = 2.5\times10^{-9}\,{\rm erg\,cm^{-2}\,s^{-1}}$, was obtained.

3.1 Hybrid Comptonization models

In the following, we present the results of the broad-band spectral analysis using the physical hybrid thermal/non-thermal Comptonization models: i.e. EQPAIR (Coppi 1999) and BELM (Belmont, Malzac & Marcowith 2008).

3.1.1 Unmagnetized model

First, we fit the broad-band spectrum with the hybrid thermal/non-thermal model EQPAIR (Coppi 1999). In this model, the emission of the disc/corona system is assumed to arise from a spherical, homogeneous, isotropic, hot ionized plasma cloud with continuous injection of relativistic electrons illuminated by soft photons emitted by the accretion disc. The model takes into consideration Compton scattering, $e^{\pm}$ pair production and annihilation, Coulomb interactions, and bremsstrahlung processes. The electron distribution at low energies is Maxwellian, with an electron temperature $kT_{\rm e}$, whereas at high energies the electrons are characterized by a non-thermal distribution. The properties of the plasma are defined by the non-dimensional compactness parameter

$$l = \frac{\sigma_{\rm T}}{m_{\rm e}c^3}\frac{L}{R}$$

where $\sigma_{\rm T}$ is the Thomson cross-section, $m_{\rm e}$ the electron mass, c the speed of light, L is the total power of the source supplied to soft seed photons and electrons, and R is the radius of the emitting region. For a detailed description of the model parameters, we refer to Coppi (1999). Since the source was in a bright HS (see fig. 2 in Bassi et al. 2019), most of the luminosity comes from the corona and the contribution of the accretion disc would be small, or negligible. Following the assumption made in previous spectral analyses of Cyg X–1 and GX 339−4 (Gierliński et al. 1999; Del Santo et al. 2008, respectively) we fixed the soft photon compactness $l_{\rm s}$, which is proportional to the luminosity of the thermal disc radiation entering the corona, to $l_{\rm s} = 10$. It is worth noticing that the predicted spectral shape is not sensitive to $l_{\rm s}$ but depends mostly on the compactness ratios

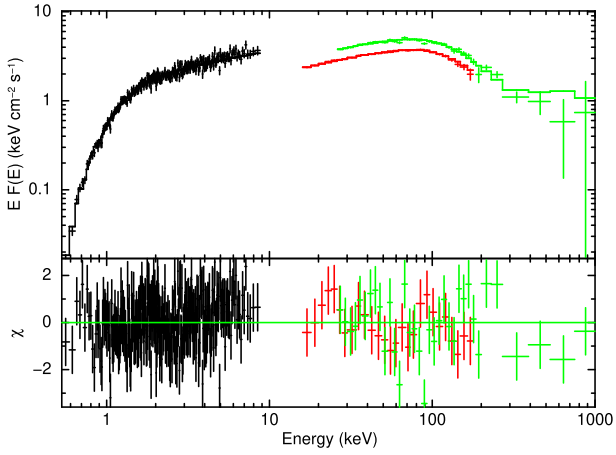

Figure 1. Broad-band energy spectra of XRT pointing #12 (black points) with average BAT (red points) and SPI (green points) spectra in the simultaneous time interval (57792.968–57793.975 MJD) fitted with the EQPAIR model.

(1) $l_{\rm h}/l_{\rm s}$, where $l_{\rm h}$ is proportional to the total power provided to the electrons of the plasma;

(2) $l_{\rm nth}/l_{\rm h}$, the fraction of the total power used to accelerate non-thermal electrons over the total power supplied to the plasma, (i.e. including also the thermal heating of the electrons $l_{\rm th}$, $l_{\rm h} = l_{\rm nth}+l_{\rm th}$).

Since the soft component is weak, constraining the seed photon temperature ($kT_{\rm max}$) makes the fit unstable, so we kept this parameter frozen at a typical value observed in this state, i.e. 0.3 keV. The non-thermal electrons are injected with a power-law distribution $\gamma^{-\Gamma_{\rm inj}}$, with a Lorentz factor γ in the range 1.3–1000. Because of the degeneracy of the parameters, following Del Santo et al. (2016), we fixed the slope of the electron distribution at the value $\Gamma_{\rm inj} = 2.5$ expected in shock acceleration models. Introducing a reflection component in the spectral model did not improve the fit significantly, therefore we fixed the reflection amplitude ($\Omega/2\pi$) at zero.

In Fig. 1, we show the best-fitting model of the broad-band spectrum. The best-fitting parameters are reported in Table 2.

The best-fitting hydrogen column density is compatible with the value obtained by Bassi et al. (2019). The $l_{\rm h}/l_{\rm s}$ values are close to the values measured for other BHBs in bright hard and intermediate states: i.e. GX 339−4 (Del Santo et al. 2008), Cyg X–1 (Del Santo et al. 2013), and Swift J174510.8−262411 (Del Santo et al. 2016). The best-fitting parameters suggest that about half of the total power is supplied to the plasma in the form of non-thermal electrons (see Table 2).

3.1.2 Magnetized model

The second hybrid thermal/non-thermal Comptonization model adopted to fit the data of GRS 1716−249 is BELM (Belmont et al. 2008). This model, in addition to the processes considered in EQPAIR, takes also into account the magnetic field in the corona and the self-absorbed synchrotron emission from the energetic leptons of the Comptonizing plasma. The effects of magnetic field are quantified through the magnetic compactness parameter

$$l_B = \frac{\sigma_{\rm T}}{m_{\rm e}c^3} R \frac{B^2}{8\pi}. \quad (1)$$

Table 2. The best-fitting parameters of the broad-band XRT, BAT, and SPI spectrum performed with an absorbed thermal/non-thermal Comptonization EQPAIR and BELM models. (1) the ratio of the total power provided to the electrons of the plasma to the soft radiation coming from the accretion disc and entering in the corona, (2) the ratio of the fraction of power used to accelerate non-thermal electrons to the total power supplied to the plasma (frozen to unity in the case of the BELM model); (3) optical depth of ionized electrons and (4) total Thomson optical depth, (5) hydrogen column density in units of 10^{22} cm^{-2}, (6) Comptonizing electron temperature in keV, (7) slope of the power-law distribution of the injected non-thermal electrons, (8) the magnetic compactness over the fraction of the power used to accelerate non-thermal electrons, (9) unabsorbed bolometric flux (0.1–1000 keV), and (10) the reduced χ^2.

	l_h/l_s	l_{nth}/l_h	τ_p	τ_T	N_H (10^{22} cm^{-2})	kT_e (keV)	Γ_{inj}	l_B/l_{nth}	Flux (erg cm^{-2} s^{-1})	χ^2_r(dof)
	(1)	(2)	(3)	(4)	(5)	(6)	(7)	(8)	(9)	(10)
EQPAIR	$9.69^{+0.31}_{-0.21}$	$0.57^{+0.04}_{-0.01}$	$1.79^{+0.08}_{-0.03}$	∼2.6	0.71 ± 0.01	∼30	(2.5)	–	4.5×10^{-8}	1.03(334)
BELM	–	1	–	3.3 ± 0.1	0.70 ± 0.02	∼34	$2.64^{+0.20}_{-0.14}$	$0.017^{+0.016}_{-0.006}$	4.6×10^{-8}	0.94(341)

Power is provided to the system in the form of a continuous injection of electrons in the corona with a power-law energy distribution $\gamma^{-\Gamma_{inj}}$ ($1 < \gamma < 1000$). At the same time electrons are removed from the overall distribution to ensure that the number of particles is conserved and mimic a non-thermal acceleration process. Malzac & Belmont (2009) showed that particles accelerated through non-thermal mechanisms can be thermalized efficiently on time-scales shorter than the light crossing time of the corona under the effects of the synchrotron boiler (Ghisellini, Guilbert & Svensson 1988; Haardt, Maraschi & Ghisellini 1994) as well as Coulomb collisions. So that, in the end the equilibrium distribution is a hybrid distribution similar to that assumed in EQPAIR. However, unlike EQPAIR where the electron energy distribution at low energies is assumed to be Maxwellian, in BELM the thermalization process is treated self-consistently.

We computed a table for a pure SSC model, where the protons are cold ($l_c = 0$), all the power is injected in the form of non-thermal particles, and the external photons (i.e. from the disc) are negligible ($l_s = 0$). Also in this model the spectral shape depends mostly on the ratio l_B/l_{nth} and is relatively insensitive to the value of the individual parameters. Under these conditions, the soft, self-absorbed synchrotron emission produced by the interaction between the non-thermal electrons and the magnetic field (B) peaks around a few eV. This component is then Compton upscattered by the hybrid thermal/non-thermal electron distribution, extending the spectrum up to the X-/γ-ray energies.

The broad-band spectrum and the different components' contributions to the model are shown in Fig. 2 and the best-fitting parameters are reported in Table 2. The hydrogen column density and the electron temperature are compatible with the values obtained with EQPAIR ($N_H = 0.70 \times 10^{22}$ cm^{-2} and $kT_e \sim 34$ keV, respectively). In the BELM model, the electron acceleration index is better constrained, so we leave it free to vary, obtaining the best-fitting value $\Gamma_{inj} = 2.64$. Then, we found a total Thompson optical depth of 3.3.

Since the spectral shape is determined by the ratio l_B/l_{nth}, the best-fitting value of l_B is highly dependent on our choice of l_{nth} and l_B does not represent the true magnetic compactness of the source. In order to estimate the observed magnetic field we need to rescale l_B to the real source compactness l_{obs}

$$l_{obs} = \frac{4\pi D^2 F \sigma_T}{R m_e c^3}, \quad (2)$$

estimated from the source luminosity. The observed magnetic field compactness can be expressed as (see Del Santo et al. 2013)

$$l_{B,obs} = \frac{l_B}{l_{nth}} \frac{l_{nth}}{l} l_{obs}. \quad (3)$$

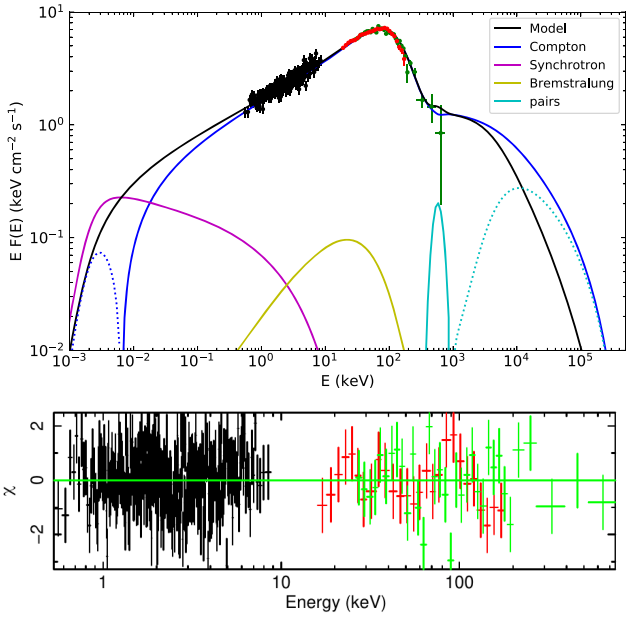

Figure 2. Top: Broad-band energy spectra of XRT pointing #12 (black points) with average BAT (red points) and SPI (green points) spectra in the simultaneous time interval (57792.968–57793.975 MJD) fitted with the BELM model. The total model (black line) corresponds to the fit of the broad-band spectrum. The positive (solid lines) and negative (dashed lines) components' contributions to the spectrum: Compton (blue), Synchrotron (magenta), bremsstrahlung (yellow), and pair annihilation/production (cyan). Bottom: Residuals obtained with the magnetized model BELM by fitting XRT, BAT, and SPI spectra.

It is worth noticing that $l = l_{nth}$ since we are considering a case of pure SSC and purely non-thermal heating of the leptons. Using equations (1) and (3), we can estimate the magnetic field B in the limit of pure SSC emission. In the case where in addition to the synchrotron photons, soft photons from the disc represent a significant source of seed photons for the Comptonization process, the efficiency of Compton cooling of the electrons in the corona is increased. Therefore, every other parameter being equal, the equilibrium temperature of the thermal electrons is lower and a steeper Comptonization spectrum with a lower energy cut-off is expected. In order to keep the model in agreement with the observed spectral shape, the Compton cooling needs to be reduced by cutting the amount of synchrotron seed photons. This can be achieved only by reducing the magnetic field. Therefore, any model combining both disc and synchrotron photons would require a magnetic field that is lower than the one given by equations (1) and (3).

Considering a pure SSC model, assuming a corona size of $R \sim 20\,R_g$ (Del Santo et al. 2013) for an $M_{BH} = 4.9\,M_\odot$ and using the estimated bolometric flux $F = 4.6 \times 10^{-8}$ erg cm^{-2} s^{-1} and the best-fitting value $l_B/l_{nth} = 0.017$ (see Table 2), we calculated an upper limit on the magnetic field in the corona $B < 1.5 \times 10^6 (\frac{20\,R_g}{R})$ G.

The magnetic field over the magnetic field in equipartition can be expressed in terms of compactness as

$$\frac{l_B}{l_{B_R}} = \frac{l_B}{l_{nth}} \frac{l_{nth}}{l} \frac{\frac{4\pi}{3}}{1 + \frac{\tau_T}{3}},$$

where l_{B_R} expresses in terms of compactness the equipartition between the magnetic field and the radiative energy density in the limit of low-energy photons ($h\nu < m_e c^2$, Lightman & Zdziarski 1987). Using this equation and the best-fitting parameters we calculated $l_B/l_{B_R} = 0.03$ for our source. Therefore, the magnetic energy density represents only a few percent at most of the radiation energy density in the corona.

4 SPECTRAL ENERGY DISTRIBUTION

4.1 The internal shock emission jet model

We used the internal shock emission model (ISHEM, Malzac 2013, 2014) to investigate whether the soft γ-ray emission (above 200 keV) detected in GRS 1716−249 by SPI can be explained as synchrotron emission from the jets.

The ISHEM model simulates the hierarchical merging of shells of plasma ejected at the base of the jet with variable velocities. A fraction of the kinetic energy of these ejecta are converted into internal energy and radiation by the shocks produced when shells of different velocities collide. The fluctuation of the Lorentz factor Γ_j of the shells in the jet is defined assuming that its power spectrum has the same shape as the PDS observed in X-ray. In presence of non-thermal acceleration processes in the jet, the synchrotron emission of the non-thermal particles generally dominates over that of the lower energy thermalized component (Wardziński & Zdziarski 2001). For this reason, the emission from the Maxwellian component of the electron energy distribution is neglected in ISHEM. We note that some authors have considered jet emission models involving only thermal relativistic electron distributions (Pe'er & Casella 2009; Tsouros & Kylafis 2017).

The model takes as input a number of parameters related to the properties of the source, the jet and the distribution of the radiating particles. In particular, for GRS 1716−249, we used a distance of 2.4 kpc (Della Valle et al. 1993) and a BH mass of $4.9\,M_\odot$ (Masetti et al. 1996). Following Malzac (2014), we defined the ejecta assuming a relativistic flow with an adiabatic index of 4/3 and a volume filling factor of 0.7. Furthermore, the jet shells are ejected from a region at the base of the jet with typical radius of $10\,R_g$ (Malzac 2014) and with a time-averaged bulk Lorentz factor Γ_{av} that is a free parameter of the model. The jet half-opening angle ϕ, the jet power P_{jet}, and the jet inclination angle ϑ are also free to vary. The electrons responsible for the synchrotron emission follow a power-law energy distribution extending in the typical XRB range from $\gamma_{min} = 1$ to $\gamma_{max} = 10^6$ (Malzac 2014), with an index of the electrons' energy distribution p.

Given a set of parameters we can compute a synthetic spectral energy distribution (SED) using the associated X-ray PSD. However, the shape of the SED is determined mostly by the power spectrum of the Lorentz factor fluctuations. The only other parameter that has an effect on the SED shape is the slope p of the power-law energy distribution of the accelerated electrons. Indeed, p affects the slope of the optically thin synchrotron emission at frequencies above the jet spectral break. In particular, the p parameter will control the jet luminosity around 1 MeV and determine whether the jet is responsible for the observed emission above 200 keV. In the following, we show the results of spectral fits with p frozen to two different values: $p = 2.5$ and $p = 2.1$ that are both in the range of values expected in shock acceleration.

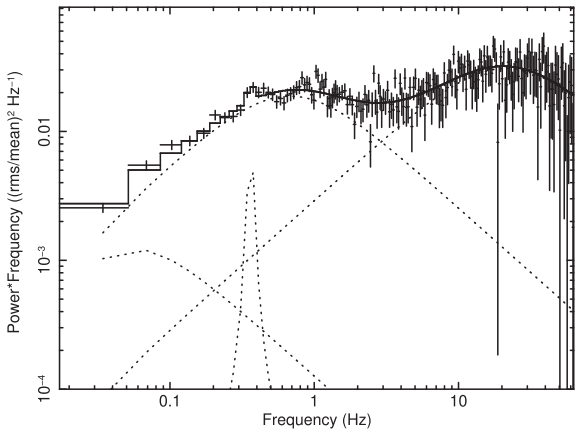

Figure 3. Average X-ray PDS of the six XRT pointings on 2018 February 9. They were fitted with three Lorentzians, of which two are zero-centred, plus a QPO.

The effect of the other parameters is to change the normalization or shift the SED along the frequency axis without altering the SED profile. If the synthetic SED shape does not fit the data there is no way to fine tune these parameters in order to match the data. On the other hand if the predicted shape of the SED is similar to the observed SED it is difficult to constrain the model parameters, as there is a strong degeneracy that makes it possible to reproduce the observed SED with many different parameter combinations. A detailed description on the behaviour of the model parameters is reported by Péault et al. (2019).

4.2 Fitting procedure

The fit of the observed SED of GRS 1716−249 was performed by following the steps below:

(i) *Compute the synthetic SED.* In order to generate the synthetic jet SED, we used the best-fitting parameters obtained for the average X-ray PDS in ISHEM and an initial set of parameters related to the source, jet, and radiating particles' properties (see Section 4.1). In Fig. 3, we show the total PDS fitted with three Lorentzians, two of which are zero-centred. A fourth Lorentzian was used to fit a QPO at 0.36 Hz (2.9σ significance). The best-fitting (χ^2_r(dof) = 1.01(178)) parameters are reported in Table 3. It is worth noting that if the X-ray QPO found in the PDS of GRS 1716−249 (see Fig. 3) is a geometrical effect due to the accretion disc precession (Motta et al. 2015), it is not related to the intrinsic aperiodic variability of the accretion flow. Therefore, it should not be introduced in the model to simulate the shells' propagation. However, the QPO is weak and its effect on the synthetic SED is negligible. Indeed, performing ISHEM simulations with and without the QPO shows that the resulting SEDs differ by no more than 4 per cent. Such small differences do not affect the analysis. Therefore, in Section 4.3 we will show the results obtained including all the four PDS components in ISHEM.

(ii) *Fit with the synthetic SED.* Once we obtained the synthetic SED, we fitted the multiwavelength data of GRS 1716−249 using

Table 3. Results of the GRS 1716−249 average XRT PDS fitted with multiple Lorentzians, given individually by $P(\nu) = r^2/\pi[\Delta^2 + (\nu - \nu_0)^2]$ (Belloni, Psaltis & van der Klis 2002). Values show the integrated rms over the full range of $+\infty$ to $-\infty$ (r), the centred frequency ν_0 and its half width at half-maximum Δ.

Lorentzian component	r	ν_0 (Hz)	Δ (Hz)
1	$0.1^{+0.01}_{-0.01}$	(0)	(0.05)
2	$12.7^{+0.9}_{-0.9}$	<2.9	$20.9^{+2.7}_{-3.1}$
3	$1.80^{+0.09}_{-0.10}$	(0)	$0.68^{+0.07}_{-0.06}$
4	$0.03^{+0.03}_{-0.06}$	$0.36^{+0.01}_{-0.01}$	$0.01^{+0.05}_{-0.02}$

the XSPEC local jet model named ISH with the break frequency and the break flux density as free parameters. This allowed us to compare the synthetic SED with the observed data and to quantify the shift in terms of frequency ($\Delta\nu$) and flux density between the synthetic and the observed SED.

(iii) *Define the reasonable parameter combinations.* For a BHB, the flux normalization and the frequency break scale as (Malzac 2013)

$$F_\nu \propto \frac{\delta^2 i_\gamma^{\frac{5}{p+4}}}{D^2 \tan\phi} \left(\frac{P_{\rm jet}}{(\Gamma_{\rm av}+1)\Gamma_{\rm av}\beta}\right)^{\frac{2p+13}{2p+8}}; \quad (4)$$

$$\nu_b \propto \frac{\delta i_\gamma^{\frac{2}{p+4}}}{\tan\phi} \left(\frac{P_{\rm jet}^{\frac{p+6}{2p+8}}}{(\Gamma_{\rm av}+1)\Gamma_{\rm av}\beta}\right)^{\frac{3p+14}{2p+8}}, \quad (5)$$

where $i_\gamma = (2-p)(\gamma_{\rm max}^{2-p} - \gamma_{\rm min}^{2-p})^{-1}$, $\beta = \sqrt{1-\Gamma_{\rm av}^{-2}}$, $\delta = [\Gamma_{\rm av}(1 - \beta\cos\vartheta)]^{-1}$ and D is the source distance.

Based on the best-fitting normalization and frequency shift parameters that we found with the ISH model, we defined a new combination of physical parameters that produced the required shift in frequency and normalization with respect to the initial model (Malzac 2013, 2014; Péault et al. 2019).

It is worth noting that in all the models, we assume that the optically thin synchrotron power law from the jet extends up to at least 1 MeV without any cooling break or high energy cut-off within the energy range covered by our observations.

4.3 Accretion and ejection emission fitting results

We assembled the observed SED of GRS 1716−249, from radio to γ-ray, from the data collected during the multiwavelength campaign.

To fit the whole SED with XSPEC, we created the spectra and the related response matrix from the ATCA, REM, and UVOT flux densities and magnitudes (see Section 2 and Table 1), by running the task FTFLX2XSP.

To fit the SED, the ISH model was used together with the irradiated disc model DISKIR (Gierliński, Done & Page 2008) to describe the contribution of the accretion flow emission and with the models REDDEN (Cardelli, Clayton & Mathis 1989) and TBABS to take into account the IR/optical and the X-ray interstellar absorption, respectively. The DISKIR model accounts for the irradiation of the outer disc and the reprocessing of the X-ray photons in the optical/UV band, in addition to the thermal Comptonization in a hot corona (Gierliński et al. 2008; Gierliński, Done & Page 2009).

Table 4. Spectral energy distribution of GRS 1716−249. The fit was performed with an irradiated disc (DISKIR) plus jet internal shock emission model (ISH). In the table we report the best-fitting values and the parameters of the simulation were obtained for a black hole of 4.9 $M_\odot$ at 2.4 kpc and assuming a jet with an electron distribution $p = 2.5$ and $p = 2.1$.

p	2.1	2.5
$\Delta\nu$	$<10^{-1.15}$	$(10^{-1.00})$
$N_{\rm H}$ (10^{22} cm^{-2})	$0.65^{+0.02}_{-0.02}$	$0.67^{+0.02}_{-0.02}$
$E(B-V)$	$0.95^{+0.25}_{-0.02}$	$1.05^{+0.18}_{-0.20}$
kT_disc (10^{-2} keV)	$4.11^{+0.01}_{-0.02}$	$5.29^{+0.73}_{-0.77}$
Γ	$1.67^{+0.01}_{-0.01}$	$1.68^{+0.01}_{-0.01}$
$kT_{\rm e}$ (keV)	50^{+4}_{-3}	58^{+3}_{-3}
$L_{\rm c}/L_{\rm d}$	>2.02	$1.72^{+3.03}_{-0.70}$
fout ($\times10^{-3}$)	$1.66^{+13.2}_{-1.5}$	>0.1
logrout	$2.54^{+0.24}_{-0.29}$	$2.56^{+0.31}_{-0.36}$
χ(dof)	1.01 (425)	1.06 (426)
ϑ	15	15
$\Gamma_{\rm av}$	4.5	4.5
ϕ	10.6	6.0
$P_{\rm jet}$ ($L_{\rm E}$)	0.04	0.05

The best-fitting parameters are shown in Table 4. Note that the goodness of our fits is mainly driven by the X-ray data. The best-fitting hydrogen column densities $N_{\rm H}$ are in agreement with the values obtained with our previous broad-band spectral fits (see Section 3.1). Moreover, the $E(B-V)$ values obtained are in agreement with the value reported by Della Valle et al. (1994) ($<E(B-V)> = 0.9 \pm 0.2$). The Comptonization parameters Γ and $kT_{\rm e}$ are similar to those typically found in HSs (see e.g. Zdziarski & Gierliński 2004; Done et al. 2007, and references therein). The ratio of luminosity in the Compton tail to that of the unilluminated disc ($L_{\rm c}/L_{\rm d}$) is higher than 1 as is expected in HS spectra. The disc emission peaks in the UV band in agreement with what is expected for a disc truncated at large radii. The outer disc radius in terms of the inner disc radius, is $R_{\rm out} \sim 10^{2.5-2.6}\,R_{\rm in}$.

4.3.1 Jet parameters

As shown in Table 4, we obtained a good fit and jet and accretion flow parameters. However, the ISHEM model with an electron distribution index p = 2.5 predicts a flux in the hard X-rays which is about one order of magnitude below the data and cannot reproduce the soft γ-ray excess detected with SPI. However, as shown in the upper panel of Fig. 4 (blue dotted line), assuming a flatter electron energy distribution ($p = 2.1$), makes the optically thin synchrotron emission harder, so matching the observed data.

Possible combinations of reasonable jet parameters corresponding to the best-fitting model are shown in Table 4. Of course, as mentioned above, the parameter degeneracy of ISHEM implies that many different combinations of parameters can fit the data equally well. For this reason the individual statistical uncertainty on each of these parameters is not meaningful and was not calculated. The degeneracy is illustrated in Fig. 5. Each point in this figure represents, a combination of jet parameters that produces the best fit of the jet SED assuming $p = 2.1$. The lines show how the jet power ($P_{\rm jet}$) and the jet half-opening angle (ϕ) change to keep a constant SED when the jet bulk Lorentz factor $\Gamma_{\rm av}$ or the inclination ϑ are varied (while all the other parameters are kept constant).

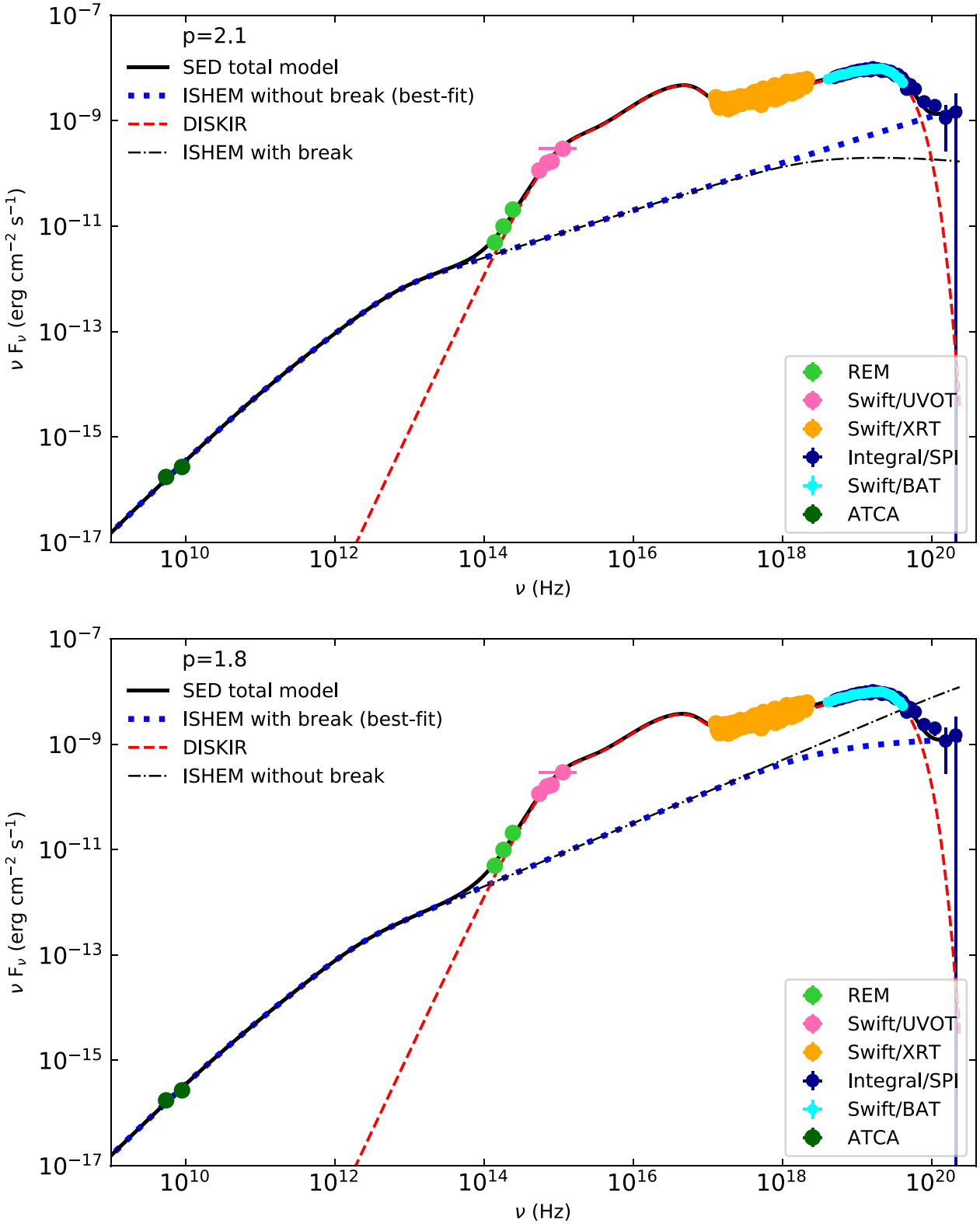

Figure 4. SED of GRS 1716−249 built with the data collected during the multiwavelength campaign performed in 2017 February and March. To reproduce the soft γ-ray emission observed (above $\sim 5 \times 10^{19}$ Hz), we used the ISHEM model assuming the electron distribution with $p = 2.1$ (upper panel) and $p = 1.8$ (bottom panel). The accretion disc/corona contribution is modelled with the irradiated disc model DISKIR (dashed red line). The blue dotted line represents, in both plots, the best fit with the jet emission model ISHEM. The black dash–dotted line shows the ISHEM model with a break at 10 keV when $p = 2.1$ (upper panel) and the ISHEM model without break when $p = 1.8$ (bottom panel). The total best-fitting model is shown as the solid black line.

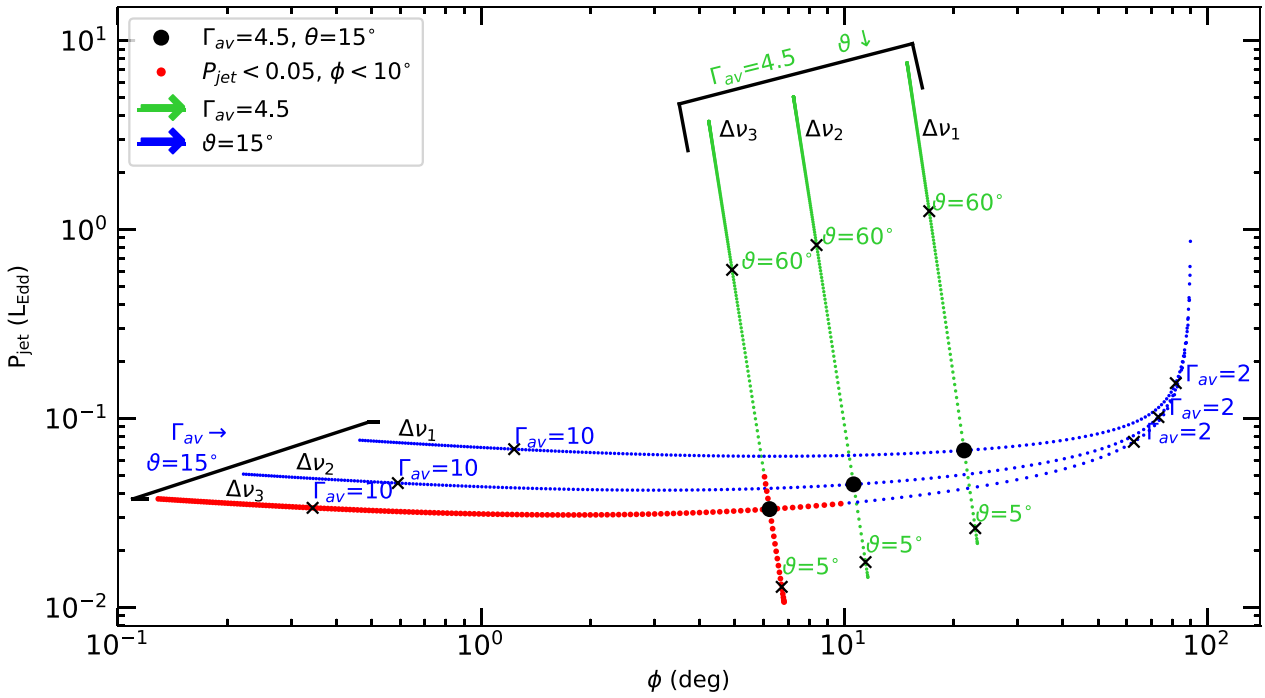

Figure 5. Evolution of the jet power ($P_{\rm jet}$) versus the jet opening angle (ϕ) as a function of the mean Lorentz factor $\Gamma_{\rm av}$ and the jet inclination angle θ assuming $p = 2.1$. We investigated the possible parameter combinations assuming three SED frequency shifts between the synthetic and observed SED: $\Delta\nu_1 = 10^{-1.5}$, $\Delta\nu_2 = 10^{-1.3}$, and $\Delta\nu_3 = 10^{-1.15}$. For each $\Delta\nu$, we assumed a fixed $\Gamma_{\rm av} = 4.5$ and vary θ from 60° to 5° (green dots). The blue dots are the evolution of $P_{\rm jet}$ versus ϕ, assuming a constant $\theta = 15°$ and varying $\Gamma_{\rm av}$ in the range 1–10. The green and blue dots show the increase of θ and $\Gamma_{\rm av}$, respectively. The red dots are the θ and $\Gamma_{\rm av}$ for which we can obtain a collimated jet ($\phi \leq 10°$) with a jet power $P_{\rm jet} \leq 0.05\, L_{\rm Edd}$.

In the case of the $p = 2.1$ model, the XSPEC fit provided only an upper limit on the frequency shift $\Delta\nu$ so the issue of degeneracy is even more stringent and we also have to consider combinations of parameters that are lower than this limit as they produce statistically comparable fits. We find that for a given ϑ and $\Gamma_{\rm av}$, a smaller shift $\Delta\nu$ results in an increasing of both ϕ and $P_{\rm jet}$ (black bullet in Fig. 5). Fig. 5 shows that, for a fixed $\Delta\nu$, small jet-opening angles (low ϕ) require large jet Lorentz factors (higher than a few). In this regime, the jet power is rather insensitive to jet Lorentz factor and opening angle. A decrease of the mean Lorentz factor requires a larger jet opening angle (high ϕ) with a slightly higher jet power (blue dots in Fig. 5). When $\Gamma_{\rm av}$ decreases below 4.5 both the jet power $P_{\rm jet}$ and opening angle ϕ start to increase significantly. When the jet opening angle exceeds ∼70°, the jet power must increase substantially to maintain the correct flux. When $\Gamma_{\rm av} \sim 2$, the jet opening angle reaches an almost constant value ∼100° and $P_{\rm jet}$ increases steeply. The decreasing ϑ at constant $\Gamma_{\rm av}$, implies slightly larger opening-angles and significantly lower jet power (green dots in Fig. 5). Reasonably, low power requires a small inclination.

Even though several parameter combinations can reproduce our data, these are not necessarily physically acceptable. Because compact jets are expected to be collimated, we favour solutions involving opening angles lower than 10° (Miller-Jones, Fender & Nakar 2006). The model of Körding, Fender & Migliari (2006) provides a simple estimate of the mean value of the jet power using the unabsorbed X-ray luminosity (see Drappeau et al. 2015; Péault et al. 2019)

$$P_{\rm jet} \approx 0.436 \left[\frac{L_{[2-10\,{\rm keV}]}}{L_{\rm Edd}}\right]^{\frac{1}{2}} L_{\rm Edd}. \quad (6)$$

The unabsorbed X-ray luminosity $L_{[2-10\,{\rm keV}]} \sim 0.01\, L_{\rm Edd}$, resulting in a jet power of about $0.05\, L_{\rm Edd}$. It is worth noticing that equation (6) is based on a number of assumptions (e.g. a not efficient accretion flow, the jet power corresponds to a constant fraction of the accretion rate, the variation of the accretion rate across the state transition is smooth and relatively slow) which are not necessarily true for GRS 1716−249. Therefore, the estimate gives only the approximate order of magnitude for the jet power.

These constraints in turn favour jets with $\Gamma_{\rm av} \geq 4.5$ and low jet inclination $\vartheta \leq 20°$ (red dots in Fig. 5).

5 THE COOLING BREAK ISSUE

During the gas expansion in the jet, the electron distribution is induced to evolve under the influence of the acceleration and the cooling of the electrons. The electrons are affected by two types of cooling: the adiabatic cooling caused by the expansion of the jet in the interstellar medium, and the radiative cooling caused by the emission of synchrotron photons. These two cooling mechanisms induce two different slopes for the electron energy distribution. At low electron energies adiabatic expansion dominates while at higher energies radiation losses constitute the main cooling mechanisms. This leads to a steepening of the lepton energy distribution at an energy corresponding to the transition between these two cooling regimes. This causes the appearance of a spectral break in the optically thin synchrotron spectrum. The presence of such a cooling break may strongly affect the high energy emission of the jet. Up to now, a direct detection of the cooling break has only been obtained for MAXI J1836−194 (Russell et al. 2014), since it is usually hidden beneath other components.

The current version of the ISHEM model does not take into account the radiation losses and therefore does not account for the presence of the cooling break. Nevertheless, we can obtain a simple estimate of the energy of the cooling break in order to check whether it would affect our fit of the SED of GRS 1716−249. Assuming a constant injection of electrons described by a power law and constant adiabatic cooling during ejection, the stationary electron distribution as a function of energy γ, can be written as

$$N(\gamma) = \frac{S_0 \tau_a}{p-1} \frac{\gamma^{-p}}{\frac{\tau_a \gamma}{\tau_s} + 1}, \quad (7)$$

where τ_a and τ_s are the characteristic adiabatic and synchrotron cooling times, respectively, defined according to the following relationships (Rybicki & Lightman 1979):

$$\tau_a = \frac{3z}{2\Gamma_{av}\beta_{av}c}, \quad (8)$$

$$\tau_s = \frac{6\pi m_e c}{\sigma_T B_j^2}, \quad (9)$$

where z is the position of the shock along the jet, $\beta_{av} = \sqrt{1 - \frac{1}{\Gamma_{av}^2}}$ and B_j is the magnetic field in the jet. Depending on the values chosen for τ_a and τ_s, different behaviours are observed. From equation (7), we see that the electron energy at which the slope of the electron energy distribution changes is around

$$\gamma_b(t) = \frac{\tau_s}{\tau_a}. \quad (10)$$

The ISHEM simulations provide the magnetic field profile along the jet and this allows us to estimate at the typical distance z at which most of the high energy synchrotron emission is produced and then estimate the magnetic field in this region. From this we can estimate γ_b. The electrons at this energy produce synchrotron photons at a typical frequency

$$\nu_c = \frac{3eB_j}{4\pi m_e c}\gamma_b^2, \quad (11)$$

which should correspond approximately to the observed frequency of the cooling break. In the previous fitting procedure, we have assumed that the slope of the optically thin synchrotron emission is constant up to ∼10 MeV, which implies that the cooling break should be at energies higher than 10 MeV. However, from the above estimates and for the best-fitting parameters given in Table 4 this is expected around 10 keV (∼10^{18} Hz).

In order to evaluate the effects of the cooling break in our fit, we have added a break in the XSPEC local jet ISH model. Fig. 4 (upper panel, black dash–dotted line) shows that the optically thin synchrotron emission softens above the break at 10 keV. Therefore, the ISHEM model with $p = 2.1$ can no longer reproduce the soft γ-ray emission of GRS 1716−249 once the presence of a cooling break is accounted for. Nevertheless, it is still possible to reproduce the emission above 200 keV with jet synchrotron emission but this would requires a much harder index of the electron distribution ($p < 2$). We fitted our data assuming a harder electron distribution ($p = 1.8$) and a break at 10 keV. As shown in the bottom panel of Fig. 4 (blue dotted line), the optically thin synchrotron emission matches the observed data. The best-fitting parameters and a possible combination of reasonable jet parameters corresponding to the best-fitting model are shown in Table 5.

In Fig. 6, we show the combination of jet parameters that produces the best fit of the jet SED assuming $p = 1.8$ and a break at 10 keV. As in Fig. 5, also in this case the lines show how the jet power (P_{jet}) and the jet half-opening angle (ϕ) change when the jet bulk Lorentz factor Γ_{av} or the jet inclination ϑ vary. On the other hand, in this figure the shift frequency parameter has been kept frozen ($\Delta\nu = 10^{-1.5}$). In particular, the green dots in Fig. 6 show how P_{jet} and ϕ change assuming constant values of Γ_{av}, namely 4.5, 7.8, 10, 15, and 18, when ϑ varies. Then, we fixed ϑ to values of 3°, 6°, 10°, 20°, and 40°, allowing Γ_{av} to vary (blue dots in Fig. 6).

Table 5. Best-fitting values of the SED by using the irradiated disc (DISKIR) model plus the jet internal shock emission model (ISH) taking into account a cooling break (ν_c) at 10 keV. The parameters of the simulation were obtained for a black hole of 4.9 $M_\odot$ at 2.4 kpc and assuming a jet with an electron distribution $p = 1.8$.

p	1.8
ν_c (keV)	(10)
$\Delta\nu$	($10^{-1.5}$)
N_H (10^{22} cm^{-2})	$0.64^{+0.02}_{-0.02}$
$E(B-V)$	$0.93^{+0.28}_{-0.12}$
kT_disc (10^{-2} keV)	$3.58^{+1.52}_{-1.41}$
Γ	$1.66^{+0.01}_{-0.01}$
kT_e (keV)	49^{+2}_{-2}
L_c/L_d	>4.14
fout ($\times 10^{-3}$)	<0.02
logrout	<2.73
χ(dof)	1.00(430)
ϑ	6°
Γ_{av}	10
ϕ	3.67
P_{jet} (L_E)	0.05

Similarly to what we have obtained assuming $p = 2.1$ (see Section 4.3 and Fig. 5), a decrease of the mean Lorentz factor requires larger ϕ values with a slightly higher P_{jet} (blue dots in Fig. 6). Then, decreasing ϑ at constant Γ_{av}, implies slightly larger ϕ and significantly lower P_{jet} (green dots in Fig. 6). Also in this case we favour solutions involving $\phi < 10°$ and $P_{jet} \leq 0.05\ L_{Edd}$ (red dots in Fig. 6). However, this region of the parameter space also implies extreme jet Lorentz factors $\Gamma_{av} \geq 10$ and very small inclination $\vartheta \leq 6°$ which we believe is unlikely. Overall, once the cooling break is included in the model we are not able to reproduce the data with 'reasonable' parameters.

6 DISCUSSION

The simultaneous multiwavelength campaign performed on GRS 1716−249 allowed us to explore the possible origin of its soft γ-ray emission. First, we fitted the X-/γ-ray spectrum with both the unmagnetized (EQPAIR) and the magnetized (BELM) hybrid Comptonization models. The fits showed that the non-thermal Comptonizing electrons can be responsible for the excess above 200 keV. The best fit with BELM in the limit of pure SSC, allowed us to estimate an upper limit on the magnetic field of the corona of about $1.5\times10^6(\frac{20\,R_g}{R})$ G. Furthermore, we found that the energy density of the magnetic field is not sufficient to explain the radiation observed. In fact, the ratio U_B/U_R (in terms of compactness) shows that the system is in a condition of subequipartition. A similar result was also derived for Cyg X–1 in the HS (Malzac 2012; Del Santo et al. 2013).

The results from Sobolewska et al. (2011) indicate that for luminosities higher than ∼1 per cent L_{Edd} the disc should supply

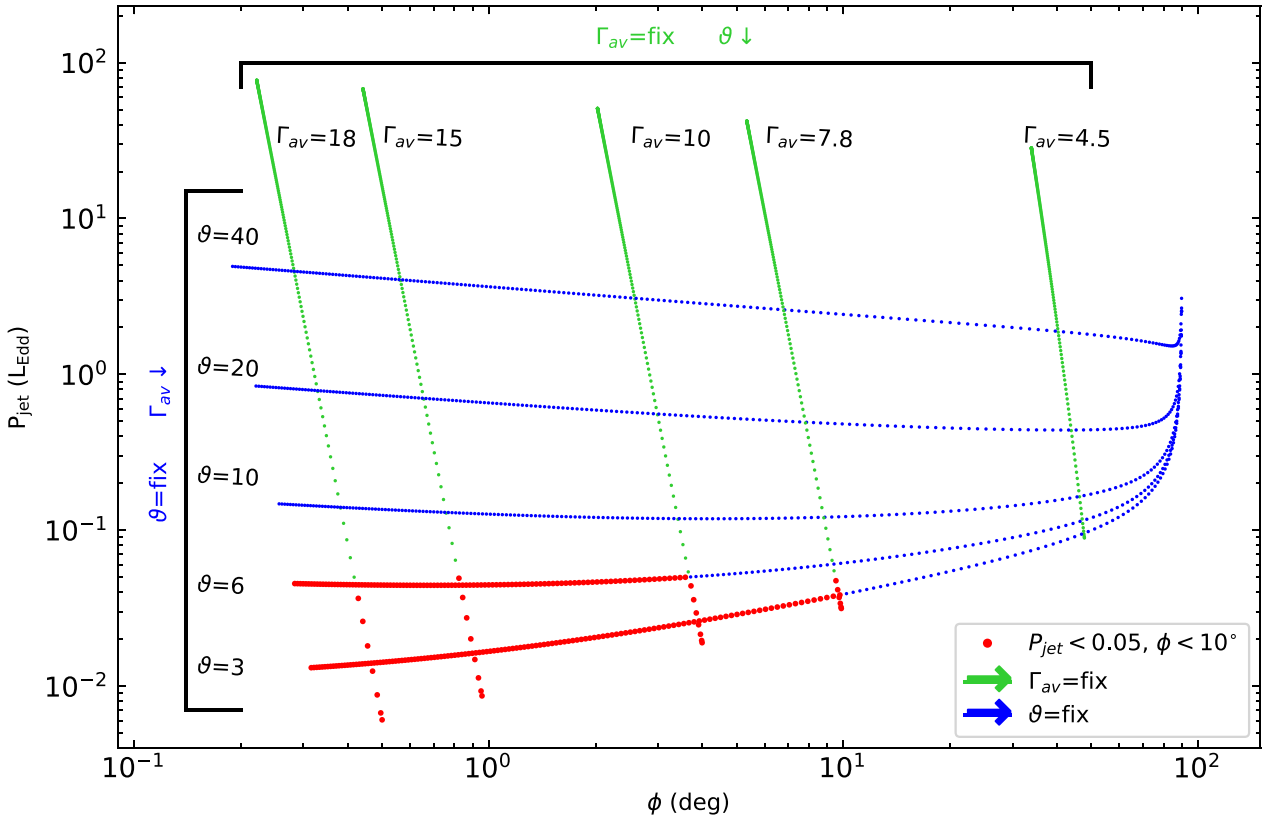

Figure 6. Evolution of the jet power ($P_{\rm jet}$) versus the jet opening angle (ϕ) as a function of the mean Lorentz factor $\Gamma_{\rm av}$ and the jet inclination angle θ assuming $p = 1.8$. We investigated the possible parameter combinations assuming a fixed $\Gamma_{\rm av} = 4.5$, 7.8, 10, 15, and 18 and a variable θ (green dots). The blue dots are the evolution of $P_{\rm jet}$ versus ϕ, assuming a constant value of θ (3°, 6°, 10°, 20°, and 40°) and varying $\Gamma_{\rm av}$ in the range 1–20. The red dots are the θ and $\Gamma_{\rm av}$ for which we can obtain a collimated jet ($\phi \leq 10°$) with a jet power $P_{\rm jet} \leq 0.05\, L_{\rm Edd}$.

the main seed photon contribution, while at lower luminosity synchrotron seed photons should dominate. The transition between these two regimes of Comptonization occurs around a luminosity that is comparable to the estimated bolometric luminosity of GRS 1716−249 ($L \sim 0.01\, L_{\rm Edd}$). Indeed, we observed that the Comptonized spectrum of GRS 1716−249 can be explained without soft seed photons from the accretion disc. If there would be an additional contribution of the seed photons from the disc, the magnetic field value should be significantly lower than the upper limit of $1.5 \times 10^6 (\frac{20\, R_{\rm g}}{R})$ G we obtained in the hypothesis of pure synchrotron seed photons.

We also investigated whether this soft γ-ray emission could be due to the jet, thus we fitted the SED of GRS 1716−249 (from radio to γ-ray) with the internal shock emission model ISHEM. We found that the jet synchrotron emission could explain the soft γ-ray emission if the index of the electron distribution is flat enough ($p \simeq 2.1$). The results support a jet with an average bulk Lorentz factor ($\Gamma_{\rm av}$) higher than 4.5 and a maximum jet inclination angle of 20° assuming reasonable values of jet opening angle ($\phi \leq 10°$, see Miller-Jones et al. 2006). The $\Gamma_{\rm av}$ we have found for GRS 1716−249 is higher than the upper limit of 2 derived from the $L_{\rm X} \propto L_{\rm R}^{0.7}$ correlation (Gallo, Fender & Pooley 2003). Even though the constraints on the bulk Lorentz factors of compact jets are few, it was shown that this correlation does not exclude high bulk Lorentz factors for BHBs jets (Heinz & Merloni 2004). Assuming that the low observed opening angles are a consequence of the transverse Doppler effect, and not due to some form of external confinement (e.g. magnetic or pressure confinement), Miller-Jones et al. (2006) showed that XRBs can produce relativistic jets with bulk speeds up to $\Gamma_{\rm av} \sim 10$, similarly to what is found in AGNs. In any case, direct constraints on this parameter have been reported in only a few cases. From the IR/X-ray lags, Casella et al. (2010) inferred a lower limit $\Gamma_{\rm av} \geq 2$ for GX 339−4 , while Tetarenko et al. (2019) constrained $\Gamma_{\rm av} \sim 2.6$ for Cyg X–1 through a radio timing analysis. Additional constraints have been reported recently by Saikia et al. (2019). These authors derived for a sample of nine BHBs bulk Lorentz factors lying in the range 1.3–3.5. Using the ISHEM model, Péault et al. (2019) inferred that the jet Lorentz factor of the compact jet in MAXI J1836−194 decreases with the hardness of the X-ray spectrum and reaches values as high as $\Gamma_{\rm av} \sim 16$ in intermediate states.

However, this jet model does not self-consistently take into account the cooling break in the jet electron distribution that we expect should be present in this source and induce a spectral steepening around 10 keV. This in fact requires a harder index of the electron distribution ($p \leq 2$). Indeed, we find that assuming $p = 1.8$ and a cooling break at 10 keV it is still possible to reproduce the soft γ-ray excess, although quite extreme jet parameters ($\Gamma_{\rm av} \geq 10$ and $\vartheta \leq 6°$) are required. Furthermore, such a hard electron distribution is difficult to reconcile with the standard shock acceleration mechanisms. Similar results were obtained by Zdziarski et al. (2014b) who modelled the γ-ray emission of Cyg X–1 using a different jet model

(Zdziarski et al. 2014a). They obtained a hard electron index ($p \sim 1.5$) that allows the formation of a hard synchrotron spectrum able to model the MeV tail (Zdziarski et al. 2014b), difficult to reconcile with the shock acceleration mechanisms. Thus, the non-thermal Comptonization process within the corona seems more likely than the jet synchrotron for the nature of the soft γ-ray emission in GRS 1716−249, unless alternative acceleration mechanisms are invoked.

7 CONCLUSIONS

In this paper, we have presented the analysis of the X-/γ-ray broadband spectra and the SED of the BHT GRS 1716−249 during its bright HS that occurred in 2017 February and March. Similarly to what has previously been observed in several sources, we detected the presence of a spectral component above 200 keV which is in excess of the thermal Comptonization spectrum.

Our results can be summarized as follow:

(i) the hybrid thermal/non-thermal Comptonization models provide a good description of the hard X-ray spectrum of GRS 1716−249. In particular, the emission above 200 keV can be explained as due to Comptonization from non-thermal electrons;

(ii) applying the ISHEM model to the radio and soft γ-ray data, we found that the emission above 200 keV can be due to the jet when the electron energy distribution has a flat slope ($p = 2.1$), which is consistent with shock acceleration mechanisms;

(iii) however, the spectral shape of the jet emission at high energy may be strongly affected by radiative cooling which is not included in the current version of ISHEM. We have estimated that in GRS 1716−249, this would lead to the formation of a spectral cooling break at roughly 10 keV. Once such a break is accounted for, it is not possible to reproduce the soft γ-ray emission with the jet model, unless the index of the electron energy distribution would be lower than 2 which is difficult to reconcile with the shock acceleration mechanisms. In addition this requires quite extreme bulk Lorentz factor (higher than 10) and very small jet inclination angle (lower than 6°).

Measurements of γ-ray polarization in BHBs would provide strong constraints on the emission processes and geometry of the flow causing the soft γ-ray emission observed in the HS.

ACKNOWLEDGEMENTS

We acknowledge financial contribution from the agreement ASI-INAF n.2017-14-H.0 and INAF main-stream (P.I. Belloni). This work also received financial support from PNHE in France and from the OCEVU Labex (ANR-11-LABX-0060) and the A∗MIDEX project (ANR-11-IDEX-0001-02) funded by the 'Investissement d'Avenir' French government program managed by the ANR. JCAM-J is the recipient of an Australian Research Council Future Fellowship (FT140101082), funded by the Australian government.

REFERENCES

Ballet J., Denis M., Gilfanov M., Sunyaev R., Harmon B. A., Zhang S. N., Paciesas W. S., Fishman G. J., 1993, Proc. IAU Circ., p. 5874
Barthelmy S. D. et al., 2005, Space Sci. Rev., 120, 143
Bassi T. et al., 2019, MNRAS, 482, 1587
Belloni T. M., Motta S. E., 2016, in Bambi C., ed., Astrophysics and Space Science Library, Vol. 440, Astrophysics of Black Holes: From Fundamental Aspects to Latest Developments. Springer-Verlag, Berlin, p. 61
Belloni T., Psaltis D., van der Klis M., 2002, ApJ, 572, 392
Belmont R., Malzac J., Marcowith A., 2008, A&A, 491, 617
Blandford R. D., Königl A., 1979, ApJ, 232, 34
Bouchet L., del Santo M., Jourdain E., Roques J. P., Bazzano A., DeCesare G., 2009, ApJ, 693, 1871
Burrows D. N. et al., 2005, Space Sci. Rev., 120, 165
Cardelli J. A., Clayton G. C., Mathis J. S., 1989, ApJ, 345, 245
Casella P. et al., 2010, MNRAS, 404, L21
Coppi P. S., 1999, in Poutanen J., Svensson R., eds, ASP Conf. Ser. Vol. 161, High Energy Processes in Accreting Black Holes. Astron. Soc. Pac., San Francisco, p. 375
Corbel S., Fender R. P., 2002, ApJ, 573, L35
Corbel S., Fender R. P., Tzioumis A. K., Nowak M., McIntyre V., Durouchoux P., Sood R., 2000, A&A, 359, 251
Coriat M. et al., 2011, MNRAS, 414, 677
Del Santo M., Malzac J., Jourdain E., Belloni T., Ubertini P., 2008, MNRAS, 390, 227
Del Santo M., Malzac J., Belmont R., Bouchet L., De Cesare G., 2013, MNRAS, 430, 209
Del Santo M. et al., 2016, MNRAS, 456, 3585
Della Valle M., Mirabel I. F., Cordier B., Bonibaker J., Stirpe G., Rodriguez L. F., 1993, Proc. IAU Circ., p. 5876
Della Valle M., Mirabel I. F., Rodriguez L. F., 1994, A&A, 290, 803
Done C., Gierliński M., Kubota A., 2007, A&AR, 15, 1
Drappeau S., Malzac J., Belmont R., Gandhi P., Corbel S., 2015, MNRAS, 447, 3832
Drappeau S. et al., 2017, MNRAS, 466, 4272
Fender R. et al., 1999, ApJ, 519, L165
Fender R. P., Pooley G. G., Durouchoux P., Tilanus R. P. J., Brocksopp C., 2000, MNRAS, 312, 853
Gallo E., Fender R. P., Pooley G. G., 2003, MNRAS, 344, 60
Gehrels N. et al., 2004, ApJ, 611, 1005
Ghisellini G., Guilbert P. W., Svensson R., 1988, ApJ, 334, L5
Gierliński M., Zdziarski A. A., Poutanen J., Coppi P. S., Ebisawa K., Johnson W. N., 1999, MNRAS, 309, 496
Gierliński M., Done C., Page K., 2008, MNRAS, 388, 753
Gierliński M., Done C., Page K., 2009, MNRAS, 392, 1106
Haardt F., Maraschi L., Ghisellini G., 1994, ApJ, 432, L95
Harmon B. A., Fishman G. J., Paciesas W. S., Zhang S. N., 1993, Proc. IAU Circ., p. 5900
Heinz S., Merloni A., 2004, MNRAS, 355, L1
Johnson W. N. et al., 1993, A&AS, 97, 21
Jourdain E., Roques J. P., 1994, ApJ, 426, L11
Jourdain E., Roques J. P., Chauvin M., Clark D. J., 2012, ApJ, 761, 27
Körding E. G., Fender R. P., Migliari S., 2006, MNRAS, 369, 1451
Laurent P., Rodriguez J., Wilms J., Cadolle Bel M., Pottschmidt K., Grinberg V., 2011, Science, 332, 438
Lightman A. P., Zdziarski A. A., 1987, ApJ, 319, 643
Malzac J., 2012, Int. J. Mod. Phys.: Conf. Ser., 8, 73
Malzac J., 2013, MNRAS, 429, L20
Malzac J., 2014, MNRAS, 443, 299
Malzac J., Belmont R., 2009, MNRAS, 392, 570
Malzac J., Jourdain E., 2000, A&A, 359, 843
Masetti N., Bianchini A., Bonibaker J., della Valle M., Vio R., 1996, A&A, 314, 123
Masumitsu T. et al., 2016, Astron. Telegram, 9895
McConnell M. et al., 1994, ApJ, 424, 933
McConnell M. L. et al., 2002, ApJ, 572, 984
Miller-Jones J. C. A., Fender R. P., Nakar E., 2006, MNRAS, 367, 1432
Motta S. E., Casella P., Henze M., Muñoz-Darias T., Sanna A., Fender R., Belloni T., 2015, MNRAS, 447, 2059
Muñoz-Darias T., Motta S., Belloni T. M., 2011, MNRAS, 410, 679
Negoro H. et al., 2016, Astron. Telegram, 9876
Nolan P. L., Gruber D. E., Knight F. K., Matteson J. L., Rothschild R. E., Marshall F. E., Levine A. M., Primini F. A., 1981, Nature, 293, 275
Pe'er A., Casella P., 2009, ApJ, 699, 1919

Péault M. et al., 2019, MNRAS, 482, 2447
Poutanen J., Coppi P. S., 1998, Phys. Scr., 77, 57
Remillard R. A., McClintock J. E., 2006, ARA&A, 44, 49
Rodriguez J. et al., 2015, ApJ, 807, 17
Roming P. W. A. et al., 2005, Space Sci. Rev., 120, 95
Roques J. P. et al., 1994, ApJS, 92, 451
Russell T. D., Soria R., Miller-Jones J. C. A., Curran P. A., Markoff S., Russell D. M., Sivakoff G. R., 2014, MNRAS, 439, 1390
Rybicki G. B., Lightman A. P., 1979, Radiative Processes in Astrophysics. Wiley, New York
Saikia P., Russell D. M., Bramich D. M., Miller-Jones J. C. A., Baglio M. C., Degenaar N., 2019, ApJ, 887, 21
Segreto A., Cusumano G., Ferrigno C., La Parola V., Mangano V., Mineo T., Romano P., 2010, A&A, 510, A47
Sobolewska M. A., Papadakis I. E., Done C., Malzac J., 2011, MNRAS, 417, 280
Stetson P. B., 1994, in Blades J. C., Osmer S. J., eds, Calibrating *Hubble Space Telescope*, Space Telescope Science Institute, Baltimore, p. 89
Stetson P. B., Vandenberg D. A., Bolte M., Hesser J. E., Smith G. H., 1989, AJ, 97, 1360
Tao L., Tomsick J. A., Qu J., Zhang S., Zhang S., Bu Q., 2019, ApJ, 887, 184
Testa V. et al., 2004, in Lewis H., Raffi G., eds, Proc. SPIE Conf. Ser. Vol. 5496, Advanced Software, Control, and Communication Systems for Astronomy. SPIE, Bellingham, p. 729
Tetarenko A. J., Casella P., Miller-Jones J. C. A., Sivakoff G. R., Tetarenko B. E., Maccarone T. J., Gand hi P., Eikenberry S., 2019, MNRAS, 484, 2987
Tsouros A., Kylafis N. D., 2017, A&A, 603, L4
Vedrenne G. et al., 2003, A&A, 411, L63
Verner D. A., Ferland G. J., Korista K. T., Yakovlev D. G., 1996, ApJ, 465, 487
Vitali F. et al., 2003, in Iye M., Moorwood A. F. M., eds, Proc. SPIE Conf. Ser. Vol. 4841, Instrument Design and Performance for Optical/Infrared Ground-based Telescopes. SPIE, Bellingham, p. 627
Wardziński G., Zdziarski A. A., 2001, MNRAS, 325, 963
Wilms J., Allen A., McCray R., 2000, ApJ, 542, 914
Winkler C. et al., 2003, A&A, 411, L1
Zdziarski A. A., Gierliński M., 2004, Prog. Theor. Phys. Suppl., 155, 99
Zdziarski A. A., Stawarz Ł., Pjanka P., Sikora M., 2014a, MNRAS, 440, 2238
Zdziarski A. A., Pjanka P., Sikora M., Stawarz Ł., 2014b, MNRAS, 442, 3243
Zdziarski A. A., Malyshev D., Chernyakova M., Pooley G. G., 2017, MNRAS, 471, 3657

This paper has been typeset from a TEX/LATEX file prepared by the author.